Magnetic Domain Imaging with Spin-Polarized SEM

24

Kazuyuki Koike

Contents

Introduction 948
Polarization of Secondary Electrons 948
Principle of Spin-SEM 951
Principle of Spin Detector 952
Configuration of the Apparatus 954
Characteristics of Spin-SEM 955
Spatial Resolution 958
Applications 962
  $Fe_{78}B_{13}Si_9$ Amorphous Ribbon 962
  $La_{1.4}Sr_{1.6}Mn_2O_7$ [46] 965
Size Limit of Magnetic Vortex Structure 966
Magnetic Coupling of Ferro- and Antiferromagnets 968
Summary 969
References 971

Abstract

In spintronics research, high-spatial-resolution, quantitative, (and in some cases) low-temperature observation of magnetic domains together with elements and crystal-direction distribution is important. As per this point of view, spin-polarized scanning electron microscopy is a significantly powerful method. In this chapter, the principle, apparatus, capabilities and some representative applications of this microscopy method are described.

K. Koike (✉)
Department of Condensed Matter of Physics, Graduate School of Science, Hokkaido University, Sapporo, Japan
e-mail: koike@phys.sci.hokudai.ac.jp

© Springer Science+Business Media Dordrecht 2016

Y. Xu et al. (eds.), *Handbook of Spintronics*,
DOI 10.1007/978-94-007-6892-5_34

List of Abbreviations	
ASTM	American Society for Testing and Materials
EBSD	Electron backscattering diffraction
SAM	Scanning Auger microscopy or scanning Auger microscope
spin-SEM	spin-polarized scanning microscopy or spin-polarized scanning microscope

Introduction

In spintronics research, magnetic domain observation with high spatial resolution is important, especially for studying nanoparticles [1], nanoparticle arrays [2], nanowires [3], thin films in the nanometer range [4], magnetic interactions between the magnetic materials [5, 6], those between magnetic materials and magnetic fields [7], spin-polarized electric current [8] and electric fields [9], materials of permanent magnets [10], half metallic materials [11], and devices such as those for magnetic random access memory [12].

There are many methods of high-resolution magnetic domain observation, including Lorentz transmission electron microscopy [13], electron holography [14], magnetic force microscopy [15], spin-polarized scanning electron microscopy (spin-SEM) [16], spin-polarized low-energy electron microscopy [17], spin-polarized photoelectron microscopy [18], transmission-type magnetic circular dichroism X-ray microscopy [19], and spin-polarized scanning tunneling microscopy [20]. Some of them are described in this handbook and also in another book [21]. Each method has its own advantages and disadvantages, so users should select the method appropriate to their purpose.

Among the methods described above, spin-SEM (this terminology is used in this chapter for both the method and the apparatus) was developed by Koike et al. [16] and is the subject of this chapter. In spin-SEM, polarization of secondary electrons emitted from a sample is detected by a spin detector and is used to form a magnetic domain image. Spin-SEM has several characteristics superior to the other methods, as described below. In this chapter, I describe this method starting from section "Polarization of Secondary Electrons" and ending with section "Applications."

Polarization of Secondary Electrons

The polarization vector $\boldsymbol{P}$ of an ensemble with n electrons is given by the average of the expectation value for the angular momentum of each electron spin $\boldsymbol{s}$ divided by $\nabla/2$:

$$\mathbf{P} = \frac{2}{\hbar}\sum_{i=1}^{n}\left\langle \varphi^{(i)} \middle| \boldsymbol{s} \middle| \varphi^{(i)} \right\rangle, \tag{1}$$

where $\varphi^{(i)}$ is a wave function of ith electron and is normalized to $\varphi^{(i)} \mid \varphi^{(i)}\text{fl} = 1$ and $\nabla = h/2\pi$ where h is the Planck constant. The relationship between $\boldsymbol{s}$ and magnetic moment $\boldsymbol{\mu}$ of the electron is given by

$$\boldsymbol{\mu} = \frac{e\hbar}{m}\boldsymbol{s} \tag{2}$$

where e and m are the charge and mass of the electron, respectively. Since e is negative, $\boldsymbol{s}$ and $\boldsymbol{\mu}$ are antiparallel and so are $\boldsymbol{P}$ and magnetization $\boldsymbol{M}$**,** which is defined by the sum of $\boldsymbol{\mu}$ in a unit volume.

The fact that the polarization of secondary electrons emitted from a ferromagnetic sample is antiparallel to the sample magnetization was found for the first time by Chrobok et al. in 1976 [22]. The possibility of magnetic domain observation using this phenomenon was proposed by DiStefano in 1978 [23], without knowing the experimental results of Chrobok et al. The relationships among the polarization, primary energy, and secondary electron energy, however, are not so simple, since the secondary electrons suffer spin-dependent inelastic scattering during the process of emission [24–26]. Figure 1 shows the secondary electron energy dependency of secondary intensity and polarization for an Fe (110) sample, for primary energies from 50 to 2,000 eV [27]. As is well known, the secondary intensity decreases exponentially with the secondary energy. The polarization also decreases with the secondary energy but reaches an almost constant value at around 20 eV. This characteristic is advantageous for spin-SEM since the polarization is larger around the energy where the intensity is higher, which gives a high signal to noise ratio S_g/N_s for spin-SEM images. This is very important since the signal is very small as described below. Figure 2 shows the primary energy dependency of secondary polarization and intensity for Fe (110) samples [28]. Here, the black squares and circles show experimental data. Solid lines are calculated results taking into account the spin-dependent inelastic mean free path. The general tendency is that when the primary energy increases, polarization also increases and reaches a constant value at around 1 keV. This characteristic is again advantageous for the same reason as above since the primary energy is usually higher than 1 keV in SEM. When high spatial resolution is required, however, the primary energy should be increased. In this case, secondary electron yield decreases and the advantage described above no longer holds. The characteristics mentioned above are common to all the 3-d magnetic materials investigated so far [29]. If we sacrifice the spatial resolution, the best S_g/N_s can be obtained at the primary energy of around 1 keV.

The information depth of magnetization of the polarized secondary electrons is important to analyze the spin-SEM image. The best way to obtain the information depth by an experiment is to measure the polarization of secondary electrons as a function of the film thickness of the magnetic material on a nonmagnetic substrate. The open circles in Fig. 3 show the results for Fe on paramagnetic FeO, where the polarization was measured during Fe evaporation at room temperature [30]. The solid line in Fig. 3 is obtained by least squares curve fitting. We assume the curve is

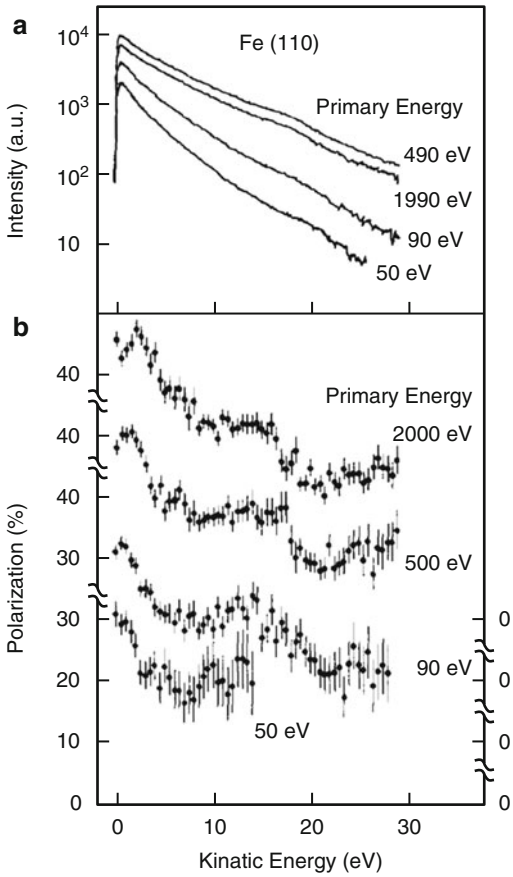

Fig. 1 Secondary electron energy dependency of secondary intensity and polarization for an Fe(110) sample, for primary energies from 50 to 2,000 eV. The larger the intensity, the larger the polarization. This is advantageous to use polarized electrons for spin-SEM since the signal to noise ratio becomes large

given by $A[1\text{-}\exp(-t/d)]$, where A and d are fitting parameters and t is the film thickness. From the obtained value of $d = 6.3$, we determine that the probing depth of magnetization is about 0.6 nm for Fe. Almost the same value of 4–5 is also obtained for Ni although the experimental method is different [31]. From these results, we can safely say that the probing depth of magnetization obtained by spin-SEM is about 0.5 nm.

Probing depth of about $d = 0.5$ nm is advantageous to observe ultrathin film [4] and surface magnetism. In addition, the samples with contamination or destroyed crystallinity layers whose thickness is less than d are observable. Samples exposed to air, however, usually have oxidized or contaminated layers thicker than d. In this case, these layers should be removed by iron spattering or by chemically reactive gas [32] depending on the sample. If the magnetism is very sensitive to the crystallinity [33], the ion spattering should be done carefully by reducing the sputtering energy.

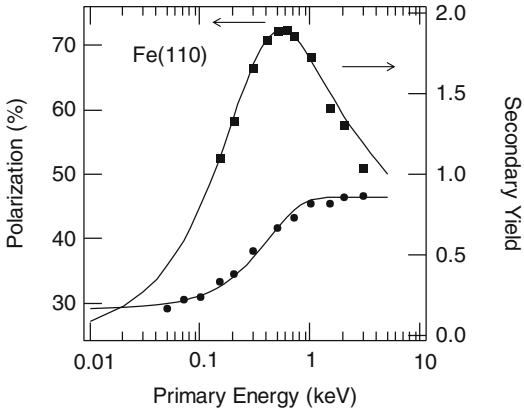

Fig. 2 Primary energy dependency of secondary polarization and intensity of Fe (110) samples. The *black squares* and *circles* show experimental data. *Solid lines* are calculated results taking into account the spin-dependent inelastic mean free path. The polarization increased with the primary energy and reaches constant value at around 1 keV. Reproduced with permission from Koike K, and Kirschner J (1992) Primary energy dependence of secondary electron polarization. J Phys D 25(7):1139–1141. Copyright 1992, IOP Publishing.

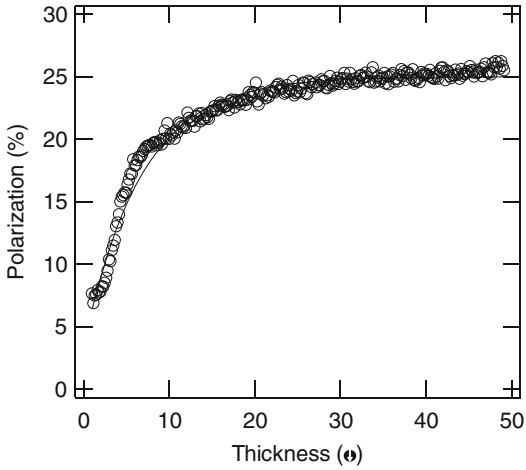

Fig. 3 Polarization of secondary electrons emitted from an Fe film deposited on paramagnetic FeO as a function of the film thickness. The *open circles* show the experimental results. The *solid line* is a fitted curve where $A[1\text{-}\exp(-t/d)]$ is assumed. From the least squares curve fitting, $d = 6.3$ is obtained, which corresponds to the magnetic information depth of polarized secondary electrons

Principle of Spin-SEM

Figure 4 shows the principle of the spin-SEM for magnetic domain observation. When a ferromagnetic sample is irradiated using a probe electron beam, electrons inside the sample, the spins of which are the origin of the magnetization, are emitted as secondary electrons while keeping their spin directions. Therefore, if we scan the

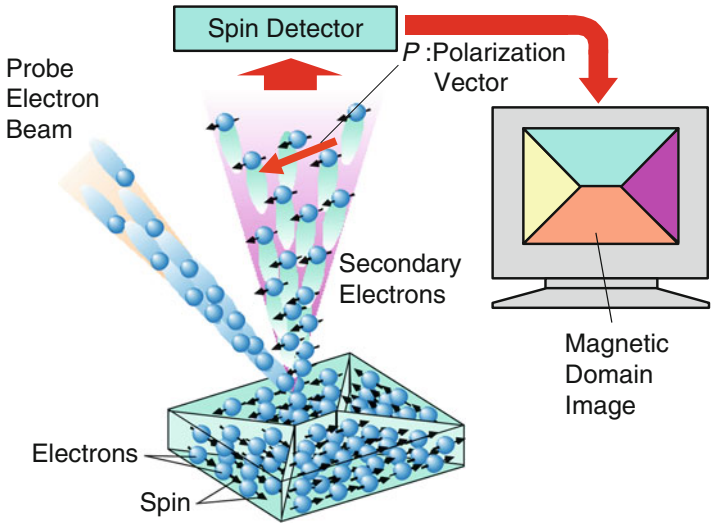

Fig. 4 Principle of the spin-SEM for magnetic domain observation. The polarization vector is parallel to the spin angular moment or antiparallel to the spin magnetic moment of secondary electrons at their originating point on the sample. By scanning the sample surface using a fine probe electron beam and detecting the polarization vector with a spin detector, a magnetic domain image is obtained

sample surface using a fine probe electron beam and detect the polarization vector of secondary electrons via a spin detector and use it as an image signal, we can obtain a magnetic domain image. Since the polarization vector is antiparallel to the magnetization vector, spin-SEM can detect the magnitude and orientation of the magnetization vector.

Principle of Spin Detector

In spin-SEM, the scattering of the electrons by heavy atoms, where spin-orbit interaction is large, is used to detect $\boldsymbol{P}$. If we define H as a Hamiltonian of the interaction, ξ as a constant determined by scattering potential, and $\boldsymbol{l}$ and $\boldsymbol{s}$ as the orbital and spin angular momentum of the scattering electrons, respectively, the H of the spin-orbit interaction is given by

$$H = \xi \boldsymbol{l} \cdot \mathbf{s}. \tag{3}$$

Figure 5 shows the principle of the spin detector using the spin-orbit interaction. When a polarized electron beam with polarization vector $\boldsymbol{P}$ is scattered by gold foil, the numbers of the backscattered electrons detected by four electron

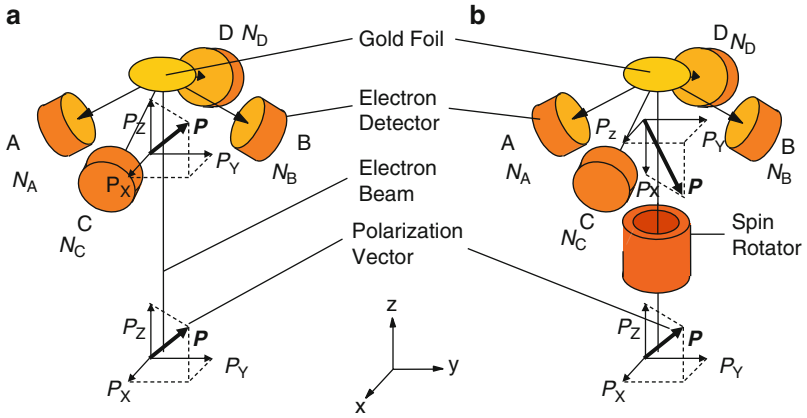

Fig. 5 Principle of the spin detector. Polarization is detected by scattering the electron beam with gold foil, where spin-orbit interaction causes asymmetry of the backscattered electron number. (**a**) Configuration for detecting polarization components P_x and P_y. (**b**) Configuration with a spin rotator for detecting P_y and P_z

detectors, A, B, C, and D located at fourfold symmetrical positions about the incident beam, are not equal as can be seen from Eqs. 1, 2 and 3. If we define these electron numbers as N_A, N_B, N_C, and N_D, in the case of Fig. 2a, the polarization vector components P_x and P_y of $\boldsymbol{P}$ defined by Eq. 1 are given by [34]

$$P_x = \frac{1}{S}\frac{N_A - N_B}{N_A + N_B}, \quad P_y = \frac{1}{S}\frac{N_C - N_D}{N_C + N_D}. \tag{4}$$

Here, S is a constant determined by the scattering condition and is typically between 0.1 and 0.3.

The z component P_z, however, cannot be detected with the geometry in Fig. 2a, since the P_z direction is perpendicular to the $\boldsymbol{l}$, and there is no contribution of P_z to the spin-orbit interaction, as can be seen from Eqs. 1, 2 and 3. For detecting the z component, we use a spin rotator [35] at the position shown in Fig. 2b. In this case, after passing through the spin rotator, the polarization vector $\boldsymbol{P}$ of electrons rotates by 90° about the y axis. Then we can detect P_z in the same way as we detect P_x:

$$P_z = \frac{1}{S}\frac{N_A - N_B}{N_A + N_B}. \tag{5}$$

In the spin-SEM application, we switch the spin rotator on and off within a pixel time. Thus, we can detect all $\boldsymbol{P}$ components P_x, P_y, and P_z substantially simultaneously [36].

Generally, the number of electrons detected in the spin detector is less than 1 % of that of electrons entering into the spin detector. Thus, the detection error due to

the statistical fluctuation becomes prominent. If we define the errors δP_x of P_x, due to the fluctuation of $N = N_A + N_B$, δP_x is given by [34]

$$\delta P_x = 1/\sqrt{S^2 \eta N_0}, \tag{6}$$

where $\hbar = N/N_0$ and N_0 is the number of electrons entering into the spin detector. From Eq. 6, we can see that if the N_0 is constant, the larger the $S^2\hbar$, the smaller the δP_x. From this consideration, we define

$$F \equiv S^2 \eta, \tag{7}$$

as the efficiency of the spin detector. The value of F used in spin-SEM is around 10^{-4}.

Here, we compare the efficiency of the spin detector with that of the electron detector used in conventional SEM. The ratio of signal S_g to noise N_s of the image signal obtained in spin-SEM is roughly

$$S_g/N_s \sim P_x/\delta P_x \sim 1/\delta P_x = \sqrt{FN_0}, \tag{8}$$

whereas that in conventional SEM is roughly

$$S_g/N_s \sim N_0/\sqrt{N_0} = \sqrt{N_0}. \tag{9}$$

From Eqs. 8 and 9, we can see that for obtaining the same S_g/N_s signal with a spin detector as with an electron detector, we need $1/F$, i.e., around 10,000 times more electrons for the spin detector than for the electron detector. Details about spin detection are covered in ▶ Chap. 22, "Spin-Resolved Valence Photoemission" of this part.

Configuration of the Apparatus

Figure 6 shows the structure of our group's newest spin-SEM, which was developed in 2009. This apparatus consists of an electron gun column equipped with a high-brightness ZrO/W Schottky emitter and an aberration corrector, a spin detector, a high-vacuum sample exchange chamber, ultrahigh-vacuum preparation chamber, and observation chamber. Attached to the preparation chamber are an ion gun, evaporator, film thickness monitor, quadrupole mass analyzer, parking lot for samples, ion pump, pressure gauge, and transfer rods. Attached to the observation chamber are a sample stage with five motion axes and a control unit for temperatures from 10 to 400 K combining a liquid helium cryostat and an electric heater, spin detector, electron backscattering diffraction (EBSD) unit, and scanning Auger microscopy (SAM) unit including an energy analyzer, ion pump, pressure gauge, and transfer rods.

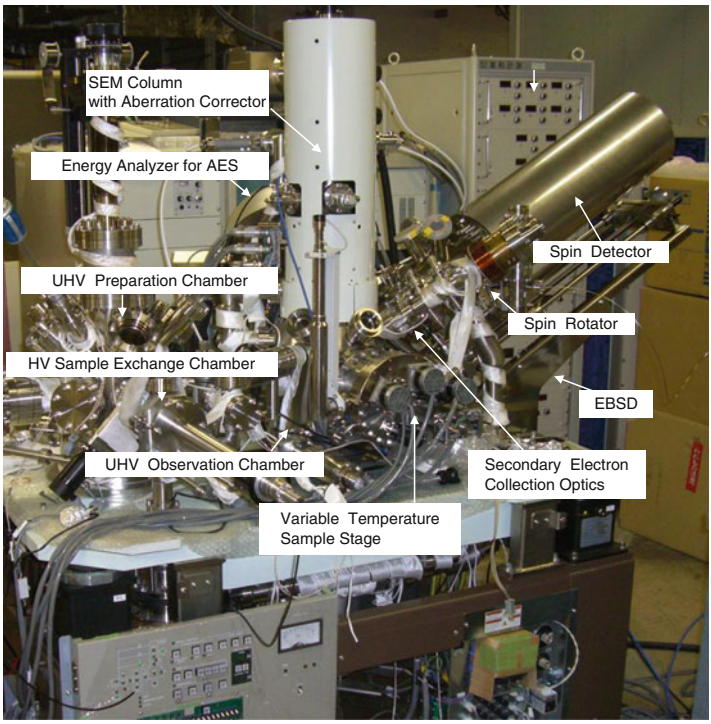

Fig. 6 Structure of the spin-SEM

Characteristics of Spin-SEM

The spin-SEM described above has the following characteristics:

1. Information obtainable for the same observation area
   1. Magnetization vector
   2. Elements
   3. Crystal direction
   4. Topography
2. Spatial resolution: 3 nm
3. Temperature: 10–400 K

Examples of characteristics 1, (1), (3), and (4), are given in section "Applications." The others are given below.

Figure 7 shows (a) Nd distribution, (b) Fe distribution, and (c) topography and magnetic domain images for the same area of an NdFeB permanent magnet. Here,

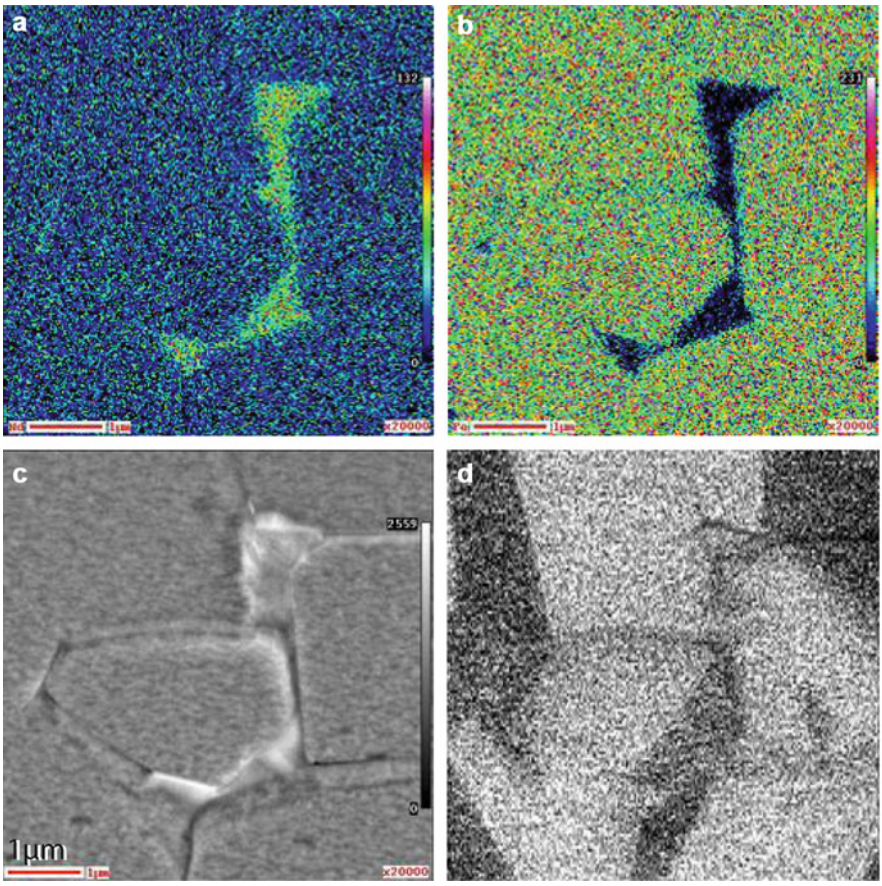

Fig. 7 (**a**) Nd distribution, (**b**) Fe distribution, (**c**) topography, and (**d**) magnetic domain images for the same area of an NdFeB permanent magnet

the element images (a) and (b) were obtained by SAM. By comparing Fig. 4a–c, the Nd-rich areas can be seen to coincide with the grain boundary regions as is already known. We can see that the domain walls run mainly inside the grains, which is not the case for soft magnetic materials such as Fe or magnetic recording media. The domain wall width is narrower for some walls, but wider for others, the reason for which is not clear at present.

Figure 8 shows (a) M_x, (b) M_y, (c) M_z, (d) topography, and (e) pseudocolor crystal direction images for the same area of an iron polycrystal. The M_x, M_y, and M_z images (a)–(c) were obtained by using magnetization components along the x, y, and z directions, respectively. The crystal direction image (e) was obtained by EBSD. The relationship between the crystal direction and color is given by the color triangle to the right of (e). The surface index of the blue grain in (d) is (111), which is the hard axis of magnetization of Fe. In this case, the domains are more

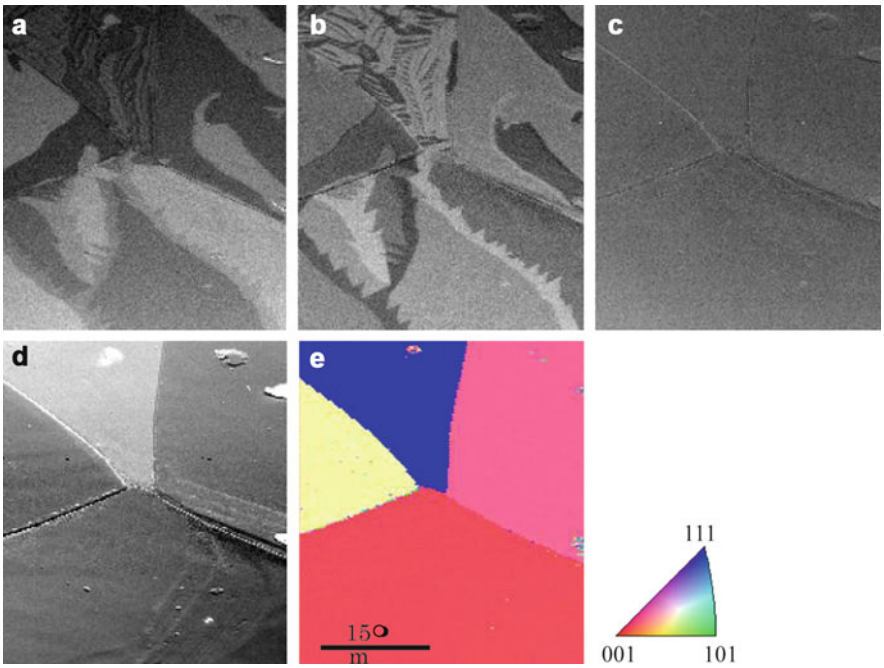

Fig. 8 (**a**) M_x, (**b**) M_y, (**c**) M_z, (**d**) topography, and (**e**) pseudocolor crystal direction images for the same area of an iron polycrystal. The M_x, M_y, and M_z images (**a**–**c**) were obtained by using magnetization components along the x, y, and z directions, respectively. The crystal direction image (**e**) was obtained by EBSD. The relationship between the crystal direction and color is given by the color triangle to the right of (**e**)

complicated and finer than the other grain surfaces, which include an easy axis of magnetization of <001> to reduce the magnetostatic energy by making closure domains at the surface. As can be seen in Fig. 8c, the surface of the Fe does not have any surface normal component of magnetization. This is the case for any soft magnetic material like Fe and a permalloy, where even bulk Bloch walls do not have a surface normal component [37–39]. An example of detailed analysis of this kind of domain structure is given in section "Applications" below.

Many of the magnetic domain observation methods provide magnetic images with a mixture of magnetic and topographic information. In these methods, the magnetic information is obtained by subtracting the topographic information from the obtained image. If the surface topography becomes large, however, this procedure no longer works. In spin-SEM, the magnetic image and topographic image are obtained by using mutually independent physical quantities: spin polarization and electric current. Thus, both images can be obtained separately [40], even for samples with a 3-dimensional surface structure. Figure 9 shows (a) magnetic, (b) topographic, and (c) the sum of magnetic and topographic images of the pole piece of a magnetic recording head for the same area obtained simultaneously by spin-SEM [41]. The magnetic image was obtained by using the magnetization

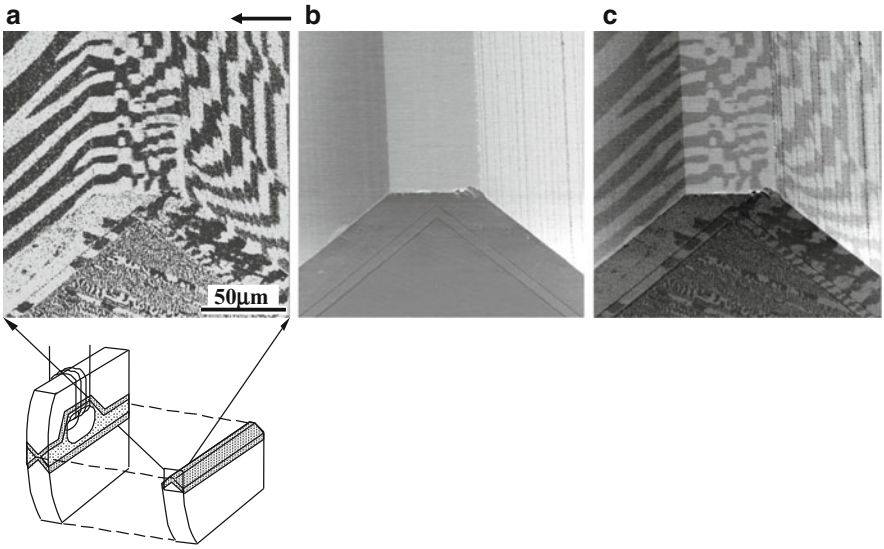

Fig. 9 (**a**) Magnetic, (**b**) topographic, and (**c**) sum of magnetic and topographic images of the pole piece of a magnetic recording head for the same area obtained simultaneously by spin-SEM

component along the arrow above the image (a). Although the sample surface has a 3-dimensional structure, we can obtain magnetic domain contrast for the whole area. The left half of the stripe domain structure in Fig. 9a is ideal for the head. However, the right half of the domain structure with the zigzag domain walls is not. In Fig. 9c, we can see that domain walls in the right half run along the black lines seen in the topography image (b), which, we speculate, are grooves formed during manufacturing process and become pinning sites of the domain walls. By optimizing the process, ideal heads will be obtained.

Spatial Resolution

As mentioned above, the efficiency of spin detector is extremely low. To overcome this difficulty and obtain a reasonable quality image, we increase the probe current I_p to around 1 nA, which is two orders of magnitude larger than that of the conventional SEM, by using a high-brightness electron emitter, and increase the diameter of the objective lens aperture. In addition, we insert the secondary electron collector between the objective lens and the sample so that we can collect as many secondary electrons as possible by increasing the working distance (WD) to around 10 mm, which is much larger than that of conventional SEM where WD is almost 0 mm. The larger aperture diameter and WD prevent reduction of the probe beam diameter, and the spatial resolution becomes lower.

Even in this situation, to obtain higher spatial resolution, we employed an aberration corrector [42]. Since the electron optical system is very different from

the conventional SEM, in the sense that the I_p of around 1 nA and WD of 10 mm are much larger than those of conventional SEM, we newly designed the corrector to correct third-order spherical and first-order chromatic aberrations, exclusively effective for special conditions mentioned above. The detailed structure will be given elsewhere [43]. In brief, it consists of four stages of 12-polar lenses, where the outer 2 lenses produce electric fields and the inner 2 lenses produce electric and magnetic fields to correct the chromatic aberration. The calculated beam diameter d without and with the corrector is shown in Fig. 10a and b, respectively, as the function beam angles for $I_p = 0.1$, 1, and 10 nA and an acceleration voltage of 20 kV. In Fig. 10a, d_S, d_C, d_D, and d_G are spherical, chromatic, and diffraction aberrations and emitter size imaged at the sample, respectively. By using these four variables, d is given by

$$d^2 = {d_S}^2 + {d_C}^2 + {d_D}^2 + {d_G}^2. \tag{10}$$

In the case of the conventional SEM with a smaller probe current, d_D is more dominant than d_G, whereas in the case of the spin-SEM with a larger probe current, d_G is more dominant than d_D. The beam diameter of 4.0 nm is obtained for $I_p = 1$ nA without the corrector as shown in Fig. 10a. In Fig. 10b, d_{S5A} and d_{S5B} are fifth-order spherical aberrations appearing due to the combination of the corrector and objective lens and that left by being uncorrected by the corrector, respectively. The beam diameter is reduced to 1.5 nm by using the corrector as shown in Fig. 7b.

The larger I_p of around 1 nA is not large enough to obtain a reasonable quality image with the same image acquisition time as that of conventional SEM, since the number of electrons is still two orders of magnitude smaller than that obtained in the conventional SEM. To compensate for the lack of electrons, we increase the image acquisition time from 10 min to 1 h in the spin-SEM, depending on the polarization of the secondary electrons.

To check the spatial resolution of the spin-SEM used in the SEM mode, we observed gold particles evaporated on a carbon block. Figure 11a shows an SEM image obtained with a probe current of 0.5 nA and acceleration voltage of 20 kV. Figure 11b shows the line profile along the red line in the white circle in Fig. 11a. By applying the ASTM E986-04 standard of 20–80 % intensity width to the line profile, we determined the spatial resolution to be 2.1 nm as shown in Fig. 11b. The resolution is lower than the calculated one. The main cause of the difference is mechanical vibration of the apparatus. To check the spatial resolution of the spin-SEM image, we observed a perpendicular recording medium. Figure 12a shows a spin-SEM image obtained with a probe current of 0.5 nA and acceleration voltage of 20 kV. The black and white band running longitudinally in the left part of the image is a recorded track with a bit length of 50 nm. Also shown in Fig. 12b is a transmission electron microscope (TEM) image of the medium. From image (b), we can see that the average size of ferromagnetic grains is around 10 nm and the width of the grain boundary that consists of nonmagnetic material is around 1 nm. The line profile of magnetization, averaged along the horizontal direction over the area surrounded by the red rectangle in Fig. 12a, is shown in Fig. 13 as black dots

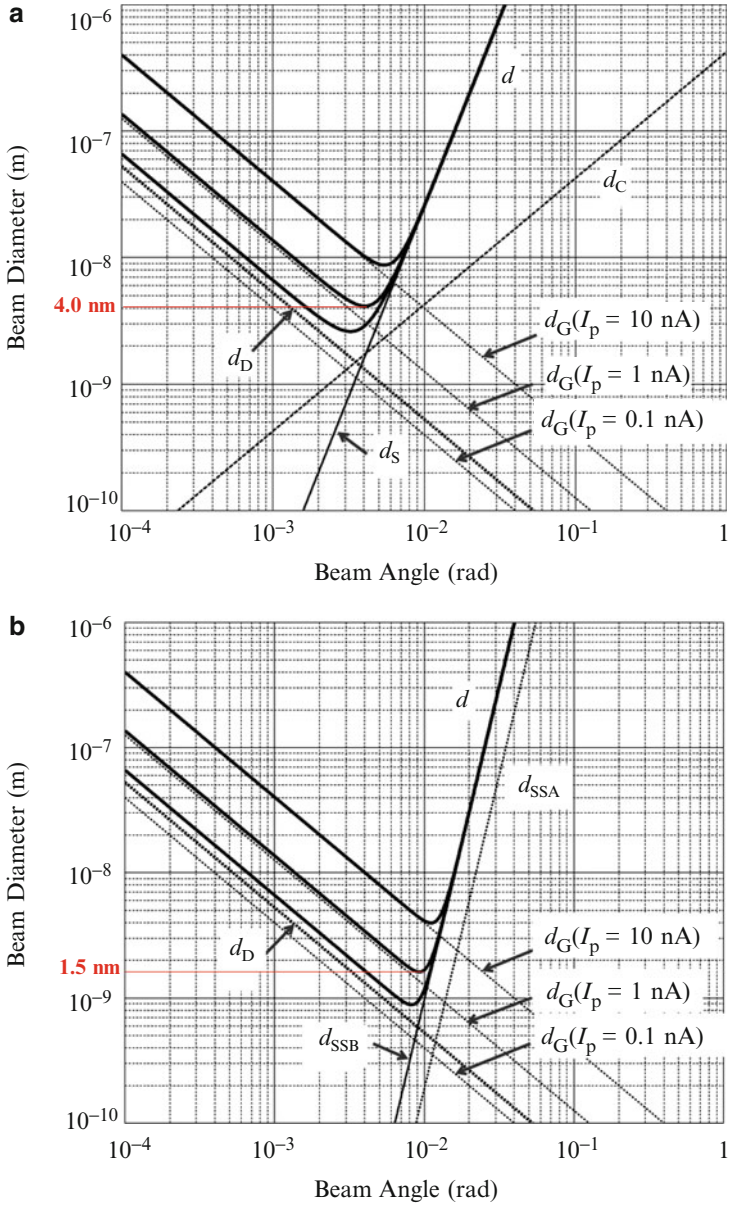

Fig. 10 Calculated beam diameter d (**a**) without and (**b**) with an aberration corrector for probe currents of 0.1, 1, and 10 nA and working distance of 10 mm. By using the corrector, the minimum beam diameter of 4 nm is reduced to 1.5 nm for the 1-nA probe current

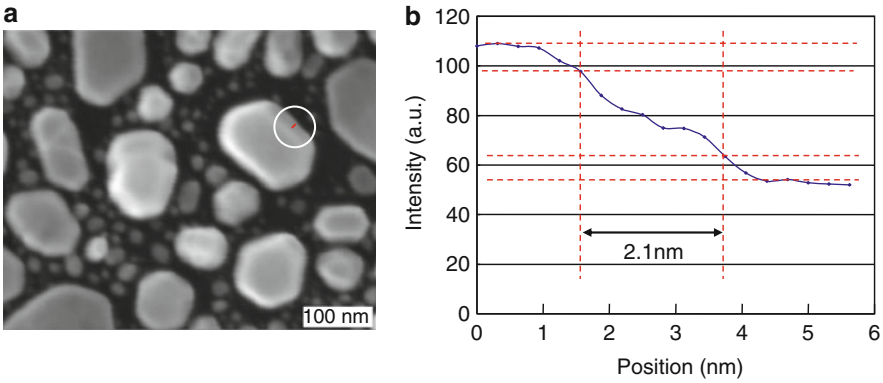

Fig. 11 (**a**) An SEM image obtained with probe current of 0.5 nA and acceleration voltage of 20 kV. (**b**) The *line* profile along the *red line* in *white circle* in (**a**). By applying the ASTM E986-04 standard of 20–80 % intensity width to the *line* profile, the spatial resolution was confirmed to be 2.1 nm

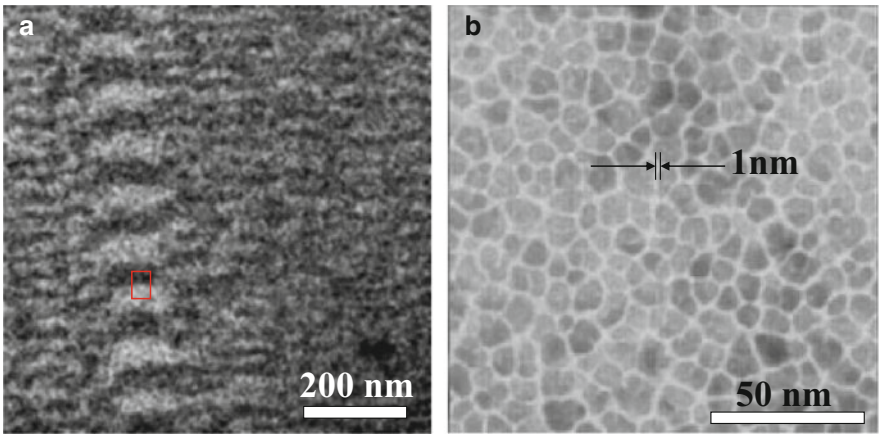

Fig. 12 (**a**) A spin-SEM image obtained with a probe current of 0.5 nA and acceleration voltage of 20 kV. The *black* and *white* band running longitudinally in the *left* part of the image is a recorded track with a bit length of 50 nm. (**b**) A transmission electron microscope image of the medium. The average size of ferromagnetic grains is around 10 nm, and the width of the grain boundary which consists of nonmagnetic material is around 1 nm

connected by a dashed line. The spatial resolution of the spin-SEM cannot be determined by the ASTM E986-04 standard since the scatter of the data in the line profile is rather large. Therefore, we conducted least squares curve fitting by convolution of the real magnetization distribution and probe beam intensity distribution. Here, we assume that the magnetization distribution is given by the inset of

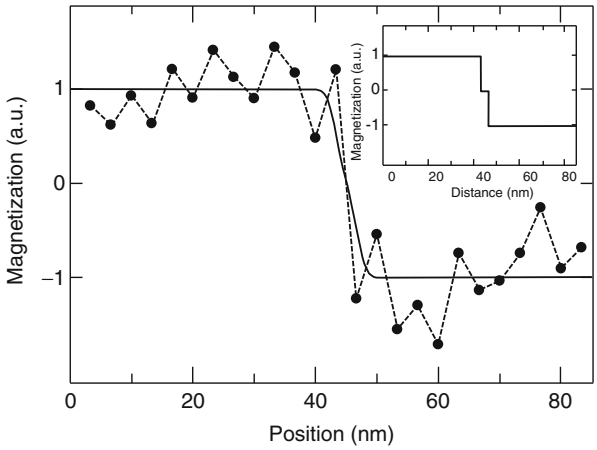

Fig. 13 The *line* profile of magnetization (*black dots* connected by *dashed line*), averaged along the horizontal direction over the area surrounded by the *red* rectangle in Fig. 12. The *solid line* is obtained by least squares curve fitting by convolution of the real magnetization distribution shown in the *inset* and the probe beam intensity of the Gaussian distribution. From the fitting result, the spatial resolution of 2.7 nm is confirmed for the spin-SEM

Fig. 13, which includes a 1-nm-wide nonmagnetic grain boundary as seen in the TEM image of Fig. 12b, the boundary runs horizontally, and the probe beam profile is Gaussian. The result is given by the solid line in Fig. 13. From the full width at half maximum of the obtained Gaussian distribution, we determined the spatial resolution of the spin-SEM to be 2.7 nm. This value is about half of the best resolution reported so far for spin-SEM [44], but lower than for the SEM image in Fig. 11a and calculated value. The cause is again mechanical vibration, which is more serious than for the SEM image because of the longer image acquisition time.

Applications

$Fe_{78}B_{13}Si_9$ Amorphous Ribbon

Figure 14 shows magnetic domain images of an as-quenched $Fe_{78}B_{13}Si_9$ amorphous ribbon [45]. The soft magnetic amorphous alloys are widely used in various MRAM as presented in Part IX of the Volume 2. The magnification increases as shown in Fig. 14a–d. In Fig. 14a, we can see large domains whose size is a few hundred micrometers and neighboring fine domains. From the magnified image of Fig. 14b, we can see that these fine domains have a stripe structure. In Fig. 14c, we can see that the stripe domain walls wave with a constant period, and there is also periodical fluctuation of magnetization inside the stripe domains. In Fig. 14d, arrows showing magnetization directions are superimposed. This sample has positive magnetostriction. Thus, the large and fine domains in Fig. 14a are formed by

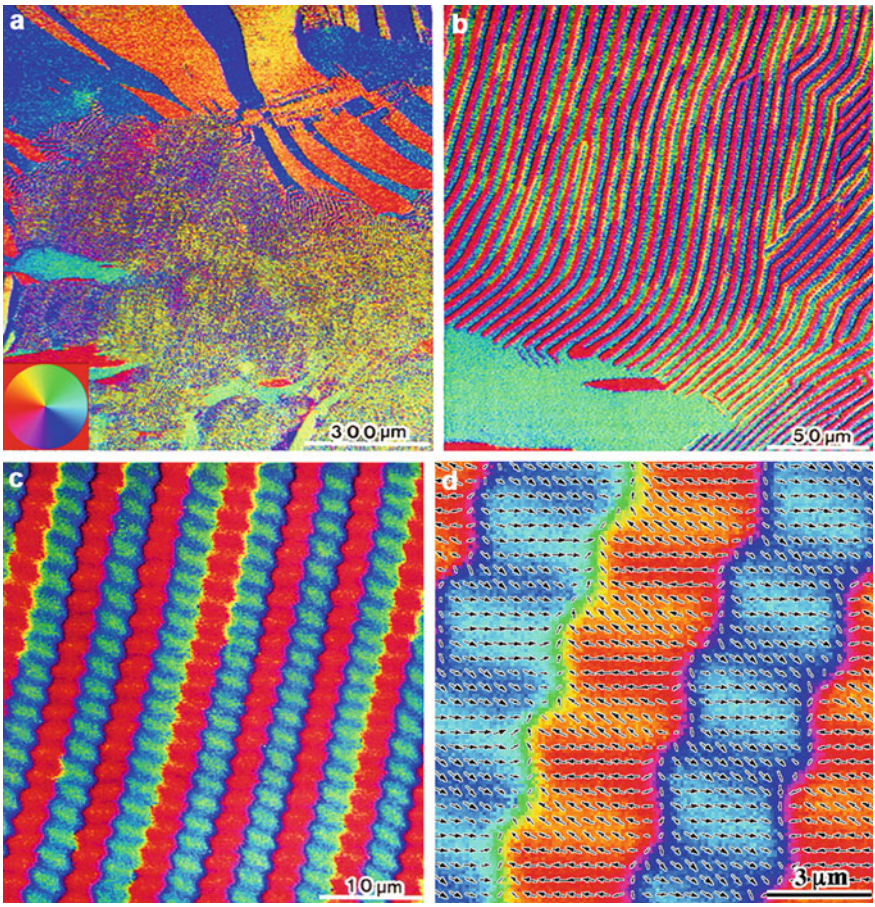

Fig. 14 Pseudocolor representation of spin-SEM images of an as-quenched $Fe_{78}B_{13}Si_9$ amorphous ribbon. The relationship between the color and magnetization direction is given by the color wheel in the *lower left corner* of (**a**). The magnification increases from (**a**) to (**d**). In (**d**), *arrows* showing magnetization directions are superimposed

uniaxial anisotropy parallel to the surface due to tensile residual stress and by perpendicular anisotropy due to compressive residual stress, respectively. As seen in Fig. 14d, the magnetization direction is perpendicular on average to the domain wall, and heads or tails of the magnetization vectors meet together at the domain walls. This structure suggests that the stripe domains are the well-known closure domains that appear at the surface to close the magnetic flux of the underlying domains. To explain the wavy domain walls and the periodic magnetization fluctuation inside the stripe, a three-dimensional domain structure model is proposed as shown in Fig. 15. In this figure, some of the domains are broken out to reveal the structural details. The domains are classified into bulk domains B with perpendicular magnetization and closure domains C at the surface. The closure domains are

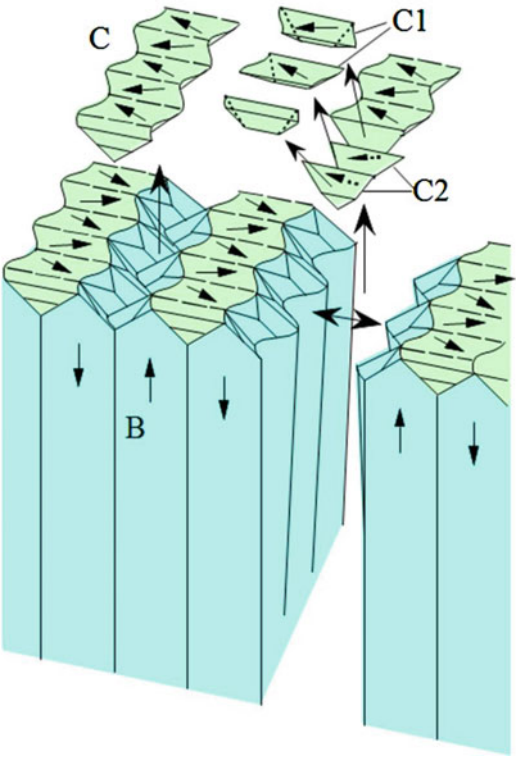

Fig. 15 Three-dimensional model of the domain structure in Fig. 14 (**d**). Some of the domains are broken out to reveal the structural details. The domains are classified into bulk domains B with perpendicular magnetization and closure domains C at the surface. The closure domains are further classified into domains C1 and C2. As a whole, the structure is a double domain closure structure composed of C1 and C2 domains. Reproduced with permission from Koike K, Matsuyama H, Tseng WJ, Li JCM (1993) Fine magnetic domain structure of stressed amorphous metal. Appl Phys Lett 62(20):2581–2583. Copyright 1993, AIP Publishing LLC

further classified into domains C1 and C2. The magnetization in the C2 domains fluctuates up and down, as shown by the dashed arrows, to reduce anisotropic energy due to perpendicular anisotropy. The C1 domains appear to prevent magnetic poles from appearing on the sample surface. To eliminate magnetic poles in the wall between the C1 and C2 domains, the wall normal component of the magnetization vector should be conserved across the wall. As a result, in-sample surface fluctuation occurs. Thus, the C1 domains are types of closure domains. The wavy walls are formed by this fluctuation. As a whole, this domain structure is a double closure structure.

The domain structure is determined to minimize total magnetic energy, i.e., the sum of wall energy, anisotropic energy, and magnetostatic energy. In the tensile stress region with in-plane surface anisotropy, the magnetizations are parallel to the surface and no magnetic poles appear on the surface. In this case, the anisotropic energy and magnetostatic energy are negligible and the domain size is determined to minimize wall energy, which results in larger domains as seen in Fig. 14a. On the other hand, in the tensile stress region with perpendicular anisotropy, the magnetizations tend to be parallel to the surface normal to minimize anisotropic energy. However, if this situation is maintained even at the surface, magnetic poles that increase the magnetostatic energy would appear. The minimum energy structure for this sample is to

form closure domains at the surface at the cost of anisotropic energy and eliminate the magnetostatic energy. The size of the closure domain is determined by the trade-off of wall and anisotropic energies; the larger (smaller) the stripe domain width, the larger (smaller) the anisotropic energy and the smaller (larger) the wall energy. The fine domains seen in Fig. 14a are formed in this way. In general, it is true that domain size is finer when easy axes of magnetization tilt from the surface, whether magnetic poles appear or not at the surface, to reduce magnetostatic energy.

$La_{1.4}Sr_{1.6}Mn_2O_7$ [46]

Figure 16 shows crystal and magnetic structures of $La_{1.4}Sr_{1.6}Mn_2O_7$ in the ground state, where the latter is determined by neutron diffraction [47, 48]. It has a multilayered perovskite structure where a metallic ferromagnetic MnO_2 bilayer in plane *ab* and a nonmagnetic insulating $(La,Sr)_2O_2$ layer are stacked alternately along direction *c* as shown in Fig. 16. It has a layered antiferromagnetic structure with perpendicular anisotropy [47] as shown by the red arrows in Fig. 16 and is a natural tunneling magnetoresistance material. It is suggested, however, that this material has a minor phase with ferromagnetism in addition to the major phase of antiferromagnetism [48]. Since the neutron diffraction obtains information from the whole sample, including both the major and minor phases, it is difficult to obtain the information only from the major phase. In this point, spin-SEM is advantageous, since it can select a single-phase area and obtain the information only from there.

We set a $La_{1.4}Sr_{1.6}Mn_2O_7$ single crystal on the sample stage of the spin-SEM, cooled it to 40 K, cleaved it, and obtained an *ab* plane with steps and terraces. The observation by spin-SEM shows that the sample has a layered antiferromagnetic structure as expected except for small areas of a ferromagnetic structure.

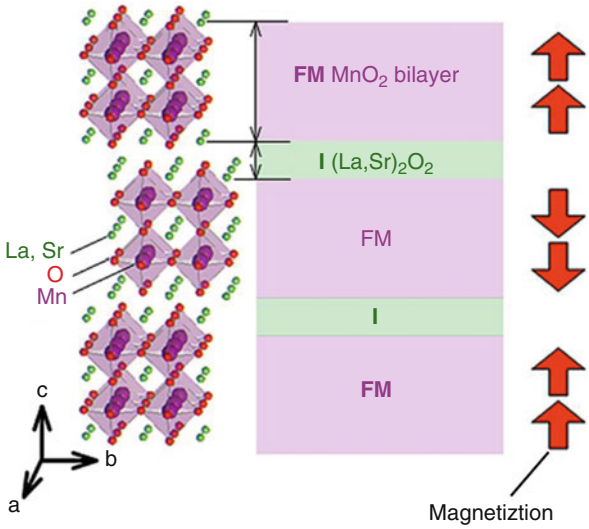

Fig. 16 Crystal and magnetic structures of $La_{1.4}Sr_{1.6}Mn_2O_7$ in the ground state. It has a multilayered perovskite structure where a metallic ferromagnetic MnO_2 bilayer in plane *ab* and a nonmagnetic insulating $(La, Sr)_2O_2$ layer are attacked alternately along direction *c*. It has a layered antiferromagnetic structure with perpendicular anisotropy

Among these, we investigated the temperature dependence of the magnetic structure for the former area. The results are shown in Fig. 17. The temperature range is from 50 to 90 K. M_x, M_y, and M_z are spin-SEM images obtained by using magnetization components along the x, y, and z directions, respectively. The black dashed lines in the M_z image at 50 K are the domain wall, since their position shifts at 60 K. The white dashed lines in the same image are steps, since their positions do not change with the temperature, and the contrast appearing between both sides of the areas in the images of M_x and M_y from 50 to 80 K confirms that the sample has a layered antiferromagnetic structure. At 70 K, the contrast in M_z disappears, while that in M_x and M_y survive until 80 K. This means that magnetization lies in the surface plane at 70 K. Since all the contrasts of M_x, M_y, and M_z disappear at 90 K, this temperature is the Neel temperature. From the polarization data in Fig. 17, the angle θ between the magnetization and the surface normal is calculated as a function of temperature and shown in Fig. 18. Kimura et al. found that the lattice contrast in the *ab* plane (*c* axis) increases (decreases) with the temperature until 80 K and decreases (increases) above that [49]. When the lattice contrast in the *ab* plane increases and that of the *c* axis decreases, the $3z^2-r^2$ orbital of e_g orbitals has lower energy than x^2-y^2, and the electron occupies the $3z^2-r^2$ orbital. In this case, the magnetization lies in plane *ab* because of spin-orbit interaction. This behavior of the lattice constant, however, has not been resolved yet.

Size Limit of Magnetic Vortex Structure

Figure 19 shows spin-SEM images of permalloy disks with a thickness of 10 nm and diameters of (a) around 300 nm and (b) around 120 nm [1]. In Fig. 18a, all the disks have a vortex domain structure, whereas in (b), all the disks have a single domain structure except the one circled by the white dashed line. The magnetic domain structure is determined by the competition of magnetostatic energy, exchange energy, and anisotropic energy. For larger magnetic materials, the multidomain structure is stable to reduce the magnetostatic energy at the cost of exchange energy [7]. However, for smaller magnetic materials, the single domain structure is stable to reduce the exchange energy or anisotropic energy at the cost of magnetostatic energy. It is important for device application to find the border size between the two. Figure 20 shows the dependence of the domain structure on both the thickness and the diameter obtained by systematic experiments. The red dots show the vortex domain structure, the red squares the single domain structure, and the triangles show a mixture of vortex and single domain structures. Thus, the border of the two structures is represented by the red dashed line. The thinner the disk, the larger the border diameter. This tendency can be explained as the thinner the disk, the lower the magnetostatic energy due to the demagnetization field. The calculated results shown by the blue triangles in Fig. 20 support this tendency, although there are quantitative discrepancies.

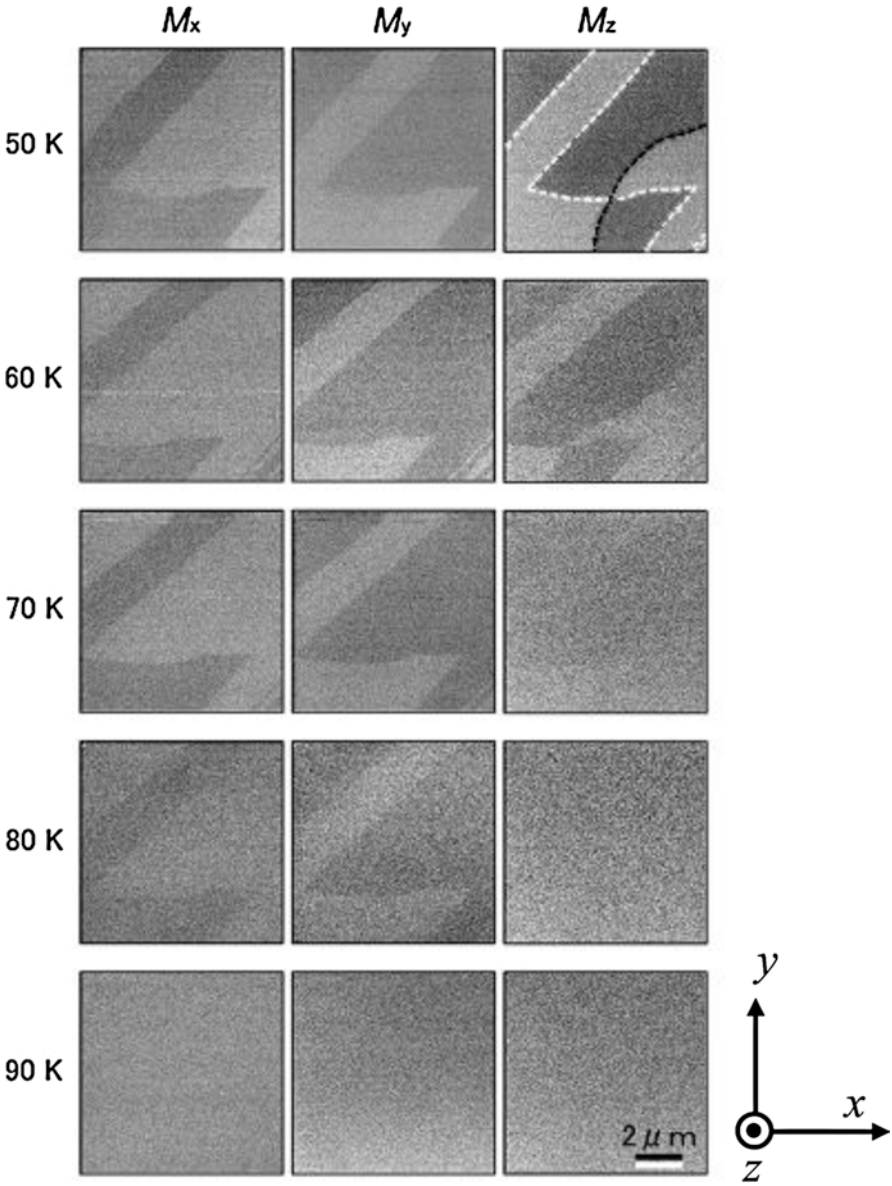

Fig. 17 Temperature dependence of magnetic structure obtained by spin-SEM. M_x, M_y, and M_z are magnetization components along the x, y, and z directions, respectively. Reprinted figure with permission from Konoto M, Kohashi T, Koike K, Arima T, Kaneko Y, Kimura T, Tokura Y (2004) Direct imaging of temperature-dependent layered antiferromagnetism of a magnetic oxide. Phys Rev Lett 93(10):107201-1-14. Copyright (2004) by the American Physical Society

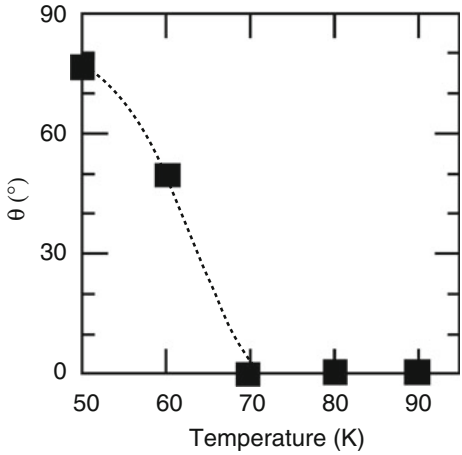

Fig. 18 Temperature dependence of the magnetization direction obtained from Fig. 18. The magnetization angle θ is measured from the sample surface normal. Copyright 2010, Japan Society of Applied Physics

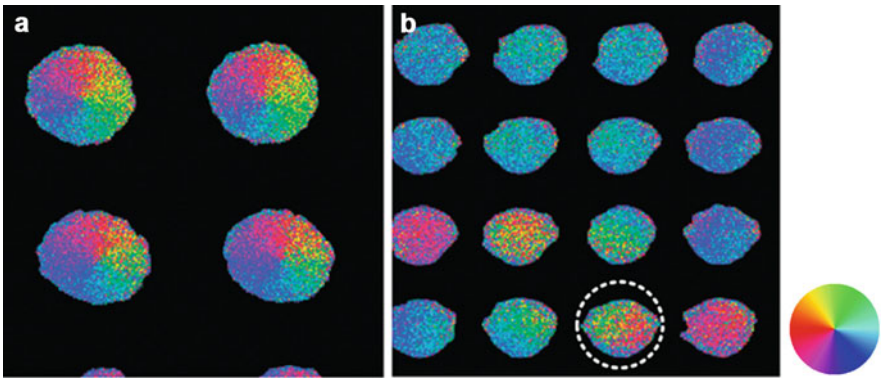

Fig. 19 Spin-SEM images of permalloy disks with a thickness of 10 nm and diameter of (**a**) around 300 nm and (**b**) around 120 nm. In Fig. 18 (**a**), all the disks have a vortex domain structure, whereas in (**b**), all the disks have a single domain structure except the one circled by the *white dashed line*. Copyright 2010, Japan Society of Applied Physics

Magnetic Coupling of Ferro- and Antiferromagnets

Exchange anisotropy, found by Meiklejohn et al., is a phenomenon in which the hysteresis loops of the stacked ferromagnet/antiferromagnet system shift in the direction of the magnetic field axis [6, 50]. This phenomenon has been successfully used in spin valve heads of hard disk drives to fix the magnetization of one of the two magnetic layers separated by a paramagnetic thin film [51]. There is, however, a debate about the mechanism of this phenomenon. A detailed discussion of the exchange bias effect is presented in ▶ Chap. 7, "Exchange Bias Material: FeMn", Part III. To study it, we obtained a spin-SEM image of 0.9-nm-thick ferromagnetic

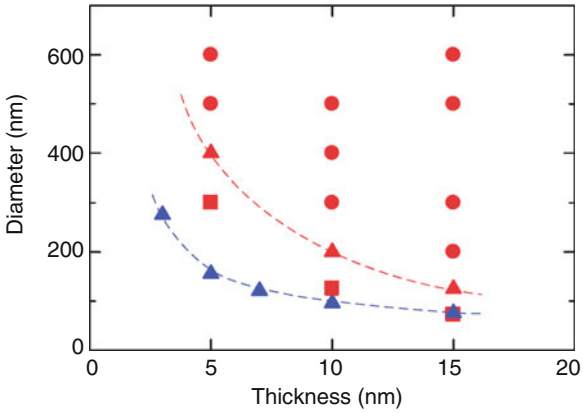

Fig. 20 Dependence of domain structure of permalloy disk on both the thickness and the diameter obtained by systematic experiments. The *red dots* show the vortex domain structure, *red squares* the single domain structure, and *red triangles* a mixture of vortex and single domain structures. The *red dashed line* is a guide for the eyes showing the border between the vortex and the single domain structures. The *blue triangles* are the calculated border, and the *blue dashed line* is a guide for the eyes. Copyright 2010, Japan Society of Applied Physics

Fe film on an antiferromagnetic NiO(001) atomically flat surface. Figure 21 shows a spin-SEM image where the arrows show the magnetization direction (left) and a topographic image (right). Since the easy planes of magnetization are {111} and easy axes of magnetization are <112>, the spins on NiO(001) are aligned antiparallel and the surface does not have net spin or is compensated. The domain structure of the Fe would be unreasonable without the interaction between the Fe film and the NiO(001), since this structure causes magnetic charges at the domain walls, and the structure would be magnetostatic-energetically unstable. The total magnetic energy calculation proposes the magnetic structure shown in Fig. 21b. The Fe spins make right angles with the easy axes of magnetization at NiO(001), although the spins of NiO(001) are slightly canted in the direction of the Fe spins. This structure results in ferromagnetic exchange interaction between the ferromagnetic Fe film and the antiferromagnetic NiO(001). This result supports the ferromagnet/antiferromagnet interaction model proposed by Koon [52]. According to this consideration, the observed Fe domain pattern in Fig. 21a is a transcription of the T domains of antiferromagnetic NiO(001).

Summary

Spin-SEM can obtain magnetic domain images by using the phenomenon that the polarization vector of secondary electrons emitted from the magnetic sample is antiparallel to the magnetization vector at their originating point on the sample. It has excellent characteristics such as high spatial resolution of around 3 nm that can be obtained by using a high-brightness emitter and aberration corrector, and all

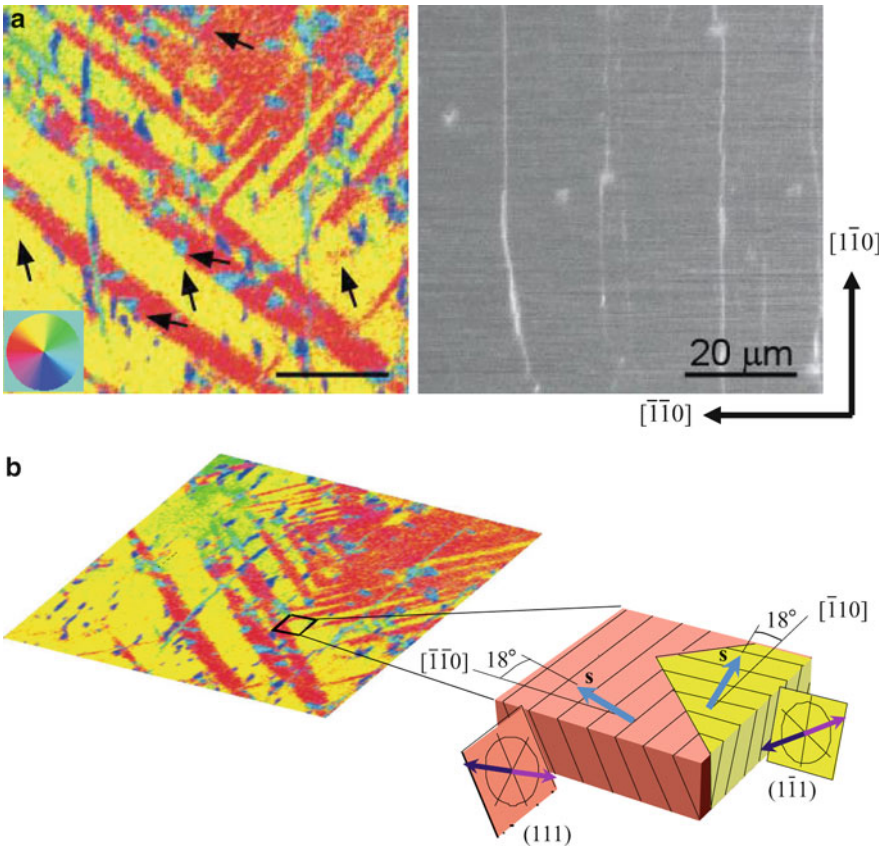

Fig. 21 (**a**) Spin-SEM image (*left*) where the *arrows* show the magnetization direction and a topographic image (*right*) of a 0.9-nm-thick ferromagnetic Fe film on an antiferromagnetic NiO (001) atomically flat surface. (**b**) Magnetic structure proposed to minimize total magnetic energy by calculation. The Fe spins make right angles with the easy axes of magnetization at NiO(001), although the spins of NiO(001) are slightly canted in the direction of the Fe spins. This structure causes ferromagnetic exchange interaction between the ferromagnetic Fe film and the antiferromagnetic NiO(001). Reprinted figure with permission from Matsuyama H, Haginoya C, Koike K (2000) Microscopic imaging of Fe magnetic domains exchange coupled with those in a NiO(001) surface. Phys Rev Lett 85(3):646–649. Copyright (2000) by the American Physical Society

three magnetization vector components or magnetization detection can be obtained by using a spin detector combined with a spin rotator. Pure magnetic images can be obtained even for samples with three-dimensional surfaces because of the independence of polarization and current, and elements and crystal direction distribution images can be obtained for the same area as the magnetic image by using Auger electrons and backscattered diffraction electrons, respectively. Some spin-SEM results obtained by application to an $Fe_{78}B_{13}Si_9$ amorphous ribbon and strongly correlated $La_{1.4}Sr_{1.6}Mn_2O_7$, permalloy nanodisks, and Fe/NiO(001) have been presented. Further applications of spin-SEM in the field of spintronics are expected.

References

1. Konoto M, Fukushima A, Matsumoto R, Kubota H, Yakushiji K, Sawa A, Yuasa S, Ando K (2010) Direct imaging of local spin orientation within artificial nanomagnets. Appl Phys Exp 3 (6):063001-1-3
2. Haginoya C, Heike S, Ishibashi M, Nakamura K, Koike K, Yoshimura T, Yamamoto J, Hirayama Y (1999) Magnetic nano-particle array with perpendicular crystal magnetic anisotropy. J Appl Phys 85(12):8327–8331
3. Sun L, Chen Q (2009) Core-shell cylindrical magnetic domains in nickel wires prepared under magnetic fields. J Phys Chem C 113(7):2710–2714
4. Speckmann M, Oepen HP, Ibach H (1995) Magnetic domain structures in ultrathin Co/Au (111): on the influence of film morphology. Phys Rev Lett 75(10):2035–2038
5. Unguris J, Celotta RJ, Pierce DT (1991) Observation of two different oscillation periods in the exchange coupling of Fe/Cr/Fe(100). Phys Rev Lett 67(1):140–143
6. Matsuyama H, Haginoya C, Koike K (2000) Microscopic imaging of Fe magnetic domains exchange coupled with those in a NiO(001) surface. Phys Rev Lett 85(3):646–649
7. Shinjo T, Okuno T, Hassdorf R, Shigeto K, Ono T (2000) Magnetic vortex core observation in circular dots of permalloy. Science 289:930–932
8. Yamaguchi A, Ono T, Nasu S, Miyake K, Mibu K, Shinjo T (2004) Real-space observation of current-driven domain wall motion in submicron magnetic wires. Phys Rev Lett 92 (7):077205-1-4
9. Fiebig M, Lottermoser T, Frohlich D, Goltsev AV, Pisarev RV (2002) Observation of coupled magnetic and electric domains. Nature 419:818–820
10. Kohashi T, Motai K, Nishiuchi T, Maki T, Hirosawa S (2009) Analysis of magnetization mechanism for NdFeB magnet using spin-polarized scanning electron microscopy (spin SEM). J Magn Soc Jpn 33(4):374–378
11. Konoto M, Kohashi T, Koike K, Arima T, Kaneko Y, Kimura T, Tokura Y (2005) Microscopy of magnetic transition in a layered manganite $La_{2-2x}Sr_{1+2x}Mn_2O_7$ (x = 0.32). Phys Rev B 71 (18):184441-1-5
12. Teixeira JM, Silva RFA, Ventura J, Pereira AM, Carpinteiro F, Araujo JP, Sousa JB, Cardoso S, Ferreira R, Freitas PP (2006) Domain imaging, MOKE and magnetoresistance studies of CoFeB films for MRAM applications. Mater Sci Eng B 126(2–3):180–186
13. Hale ME, Fuller HW, Rubinstein H (1959) Magnetic domain observation by electron microscopy. J Appl Phys 30(5):789–791
14. Tonomura A, Matsuda T, Endo J (1980) Direct observation of fine structure of magnetic domain walls by electron holography. Phys Rev Lett 44(21):1430–1433
15. Martin Y, Wickramasinghe HK (1987) Magnetic imaging by "force microscopy" with 1000 Å resolution. Appl Phys Lett 50(20):1455–1457
16. Koike K, Hayakawa K (1984) Scanning electron microscope observation of magnetic domains using spin-polarized secondary electrons. Jpn J Appl Phys 23(3):L187–L188
17. Pinkvos H, Poppa H, Bauer E, Hurst J (1992) Spin-polarized low-energy electron microscopy study of the magnetic microstructure of ultra-thin epitaxial cobalt film on W(110). Ultramicroscopy 47(4):339–345
18. Stohr J, Wu Y, Hermsmeier D, Samant MG, Harp GR, Koranda S, Dunham SD, Tonner P (1993) Element-specific magnetic microscopy with circularly polarized X-rays. Science 259:658–661
19. Fischer P, Schutz G, Schmahl G, Guttmann P, Raasch D (1996) Imaging of magnetic domains with the X-ray microscope at BESSY using X-ray magnetic circular dichroism. Z Phys B 101 (3):313–316
20. Bode M, Getzlaff M, Wiesendanger R (1998) Spin-polarized vacuum tunneling into the exchange-split surface state of Gd(0001). Phys Rev Lett 81(19):4256–4259
21. Hopster H, Oepen HP (eds) (2003) Magnetic microscopy of nanostructures. Springer, Berlin
22. Chrobok G, Hofmann M (1976) Electron spin polarization of secondary electrons ejected from magnetized europium oxide. Phys Lett 57A(3):257–258

23. DiStefano TH (1978) Technology for detecting small magnetic domains and beam-addressed memory therewith. IBM Tech Disc Bull 20(10):4212–4215
24. Hopster H, Raue R, Kisker E, Guntherodt G, Campagna M (1983) Evidence for spin-dependent electron–hole-pair excitations in spin-polarized secondary-electron emission from Ni(110). Phys Rev Lett 50(1):70–73
25. Penn DR, Apell SP, Girvin SM (1985) Theory of spin-polarized secondary electrons in transition metals. Phys Rev Lett 55(5):518–521
26. Tamura E, Feder R (1986) Theory of spin-polarized secondary electron emission from ferromagnets. Phys Rev Lett 57(6):759–761
27. Kirschner J, Koike K (1992) Spin polarization of secondary electrons from Fe(110) excited by unpolarized primary electrons. Surf Sci 273(1–2):147–159
28. Koike K, Kirschner J (1992) Primary energy dependence of secondary electron polarization. J Phys D 25(7):1139–1141
29. Koike K, Hayakawa K (1984) Spin polarization of electron-excited secondary electrons from a permalloy polycrystal. Jpn J Appl Phys 23(2):L85–L87
30. Mori K, Yamazaki M, Hiraki T, Matsuyama H, Koike K (2006) Comment on "oxidation of the Fe(110) surface: an Fe_3O_4(111)/Fe(110) bilayer. Phys Rev B 74(2):026405-1-2
31. Abraham DL, Hopster H (1987) Magnetic probing depth in spin-polarized secondary electron spectroscopy. Phys Rev Lett 58(13):1352–1354
32. Konoto M, Yamada H, Koike K, Akoh H, Kawasak M, Tokura Y (2008) Magnetic quasidomain structures in Ru-doped $La_{0.6}Sr_{0.4}MnO_3$ thin films. Appl Phys Lett 93 (25):252503-1-3
33. Koike K, Furukawa T (1996) Evidence for ferromagnetic order at the FeO(111) surface. Phys Rev Lett 77(18):3921–3924
34. Kessler J (1985) Polarized electrons. Springer, Heidelberg
35. Kohashi T, Konoto M, Koike K (1995) A spin rotator for detecting all three magnetization vector components by spin-polarized scanning electron microscopy. Jpn J Appl Phys 66 (12):5537–5543
36. Kohashi T, Konoto M, Koike K (2004) A spin rotator for spin-polarized scanning electron microscopy. Rev Sci Instrum 75(6):2003–2007
37. LaBonte AE (1969) Two-dimensional Bloch-type domain walls in ferromagnetic films. J Appl Phys 40(6):2450–2458
38. Koike K, Matsuyama H, Hayakawa K, Mitsuoka K, Narishige S, Sugita Y, Shiiki K, Saka C (1986) Observation of neel structure walls on the surface of 1.4-mm-thick magnetic films using spin-polarized scanning electron microscopy. Appl Phys Lett 49(15):980–981
39. Oepen HP, Kirschner J (1989) Magnetization distribution of 180 domain walls at Fe(100) single-crystal surfaces. Phys Rev Lett 62(7):819–822
40. Koike K, Hayakawa K (1984) Observation of magnetic domains with spin-polarized secondary electrons. Appl Phys Lett 45(5):585–586
41. Koike K, Matsuyama H (1991) A data-acquisition and display system for spin-polarized scanning electron microscopy (spin-SEM). Rev Sci Instrum 62(4):970–981
42. Zach J, Haider M (1995) Aberration corrector in a low voltage scanning microscope. Nucl Instrum Method Phys Res A 363(1–2):316–325
43. Hososkawa M, Kato M, Tazawa T, Koike K (unpublished)
44. Kohashi T, Koike K (2001) Spin-polarized scanning electron microscope with 5-nm resolution. Jpn J Appl Phys 40(11B):L1264–L1266
45. Koike K, Matsuyama H, Tseng WJ, Li JCM (1993) Fine magnetic domain structure of stressed amorphous metal. Appl Phys Lett 62(20):2581–2583
46. Konoto M, Kohashi T, Koike K, Arima T, Kaneko Y, Kimura T, Tokura Y (2004) Direct imaging of temperature-dependent layered antiferromagnetism of a magnetic oxide. Phys Rev Lett 93(10):107201-1-14
47. Perring TG, Aeppli G, Kimura T, Tokura Y, Adams MA (1998) Ordered stack of spin valves in a layered magnetoresistive perovskite. Phys Rev B 58(22):R14693–R14696

48. Argyriou DN, Mitchell JF, Radaelli PG, Bordallo HN, Cox DE, Medarde M, Jorgensen JD (1999) Lattice effects and magnetic structure in the layered colossal magnetoresistance manganite La_{2-2x} $Sr_{1+2x}Mn_2O_7$, x = 0.3. Phys Rev B 59(13):8695–8702
49. Kimura T, Tomioka Y, Asamitsu A, Tokura Y (1998) Phase diagram of tetragonal manganese. Phys Rev Lett 81(26):5920–9523
50. Meiklejohn WH, Bean CP (1956) New magnetic anisotropy. Phys Rev 102(5):1413–1414
51. Dieny B, Speriosu VS, Parkin SSP, Gurney BA, Wilhoit DR, Mauri D (1991) Giant magnetoresistance in soft ferromagnetic multilayers. Phys Rev B 43n:1297–1300
52. Koon NC (1997) Calculations of exchange bias in thin films with ferromagnetic/antiferromagnetic interfaces. Phys Rev Lett 78(25):4865–4868